The redistribution of anthropogenic excess heat is a key driver of warming in the North Atlantic

Marie-José Messias, Herlé Mercier

communications earth & environment

ARTICLE

https://doi.org/10.1038/s43247-022-00443-4 OPEN

The redistribution of anthropogenic excess heat is a key driver of warming in the North Atlantic

Marie-José Messias [1,3]✉ & Herlé Mercier [2,3]

Understanding ocean excess heat uptake is crucial for assessing climate warming, yet uncertainties remain about its history and redistribution. Here, we reconstruct ocean heat content change along the 25°N Atlantic hydrographic section and assess its spatiotemporal origin and fate. We show that the delayed response of the ocean below 700 m to sea surface temperature change contribute to 62% of full depth warming at this latitude for 1850–2018, falling to 35% for 1975–2018 when anthropogenic warming in the upper ocean accelerated. The regional climate fluctuations shape ocean heat content variability at 25°N with contributions from the Labrador Sea producing most of the decadal variability and the Nordic Seas bound to become the main contributor to deep ocean warming in the coming decades. Chiefly, the net excess heat transport across 25°N has increased recently, warming the domain north of 25°N at a rate of $0.89 \pm 0.19\ W\ m^{-2}$ during 2012–2018, revealing that excess heat redistribution is a key driver of North Atlantic heat gain.

[1] College of Life and Environmental Sciences, University of Exeter, Exeter EX4 4QE, UK. [2] University of Brest, Laboratoire d'Océanographie Physique et Spatiale, UMR 6523, CNRS, IUEM, Ifremer Centre de Brest, CS 10070, 29280 Plouzané, France. [3] These authors contributed equally: Marie-José Messias, Herlé Mercier. ✉email: M.Messias@exeter.ac.uk

Accurate knowledge of the temporal and regional distributions of ocean heat content change (ΔOHC) is key to monitoring the Earth energy imbalance and the anthropogenic climate perturbation[1–5]. Yet, ΔOHC is mainly assessed from the 1960s and for the upper 2000 m[6–9] where temperature records are most numerous[10–12]. For the deep ocean, ΔOHC estimates have mostly relied on decadal hydrographic surveys whose sparse observational coverage[9,11,13] makes estimates of the deep variability uncertain, particularly in the North Atlantic[14]. Historical reconstructions of ocean temperatures with the improved deep-sea resolution, such as those provided by recent studies[15–17] and the present work, are therefore essential for a full account of ocean heat uptake. Long-term and well-resolved time series are also an asset to help disentangle long-term warming due to anthropogenic forcing of the climate system from regional deviation of ocean heat content trends[18] due to internal variability such as the North Atlantic Oscillation (NAO)[19] or the Atlantic Multidecadal Oscillation (AMO)[20].

Besides accurate estimates of the full depth ΔOHC inventories in response to climate change, understanding how the ocean redistributes temperature anomalies (ΔT) absorbed at its surface is a prerequisite for improving the reconstruction of past climates and skillful climate projections[21]. Excess heat (taken as ΔOHC since a chosen reference period) redistribution from the Southern to the Northern hemisphere by the ocean circulation has been shown to balance the interhemispheric asymmetry in ocean surface heat uptake in CMIP5 historical simulations during 1861–2005[22]. Yet, observations[12,23] and models[24] show that during the recent period (2005–2015), the southern hemisphere ocean was storing more heat than the northern hemisphere ocean, with Rathore et al.[24] noting that the 2005–2015 hemispheric asymmetry in heat gain (0–2000 m) can be explained by internal climate variability. On a regional scale, most of the warming of the Arctic Mediterranean for 2002–2012 can be accounted for by an increase in northward ocean heat transport at the Greenland-Scotland Ridge[25], with transport and temperature contributing by equal parts. As unabated warming is observed[26], the role of the ocean in transporting excess heat and shaping regional patterns of heat gain is still an ongoing debate.

Here we present a new historical full-depth ΔOHC reconstruction, placing our focus on the 25°N trans-Atlantic hydrographic section, a benchmark for the quantification of the AMOC and associated heat transport[27–29]. The section benefits from frequent occupations and continuous AMOC monitoring since 2004[30,31] (Fig. 1a, Supplementary Table 1 and Supplementary Fig. 1). The reconstruction is based on time-varying sea surface temperatures (SST, monthly time series for years 0–2018) of the global ocean and Green's functions. The latter represents the ocean circulation and, convolved under the assumption of a stationary state with SST observations, allows us to reconstruct the temporal evolution of the surface-bottom temperature at 25°N ('Methods'). One advantage of the approach is that because space and time-varying history of SST is relatively well observed compared to the interior of the ocean, the reconstructed continuous and full-depth temperature time series at 25°N fill in for times when interior observations are missing. We determined the Green's functions using a maximum entropy principle (MEP) constrained by measurements of temperature and 8 other independent tracers (transient tracers, salinity and preformed nutrients) along five full-depth surveys of the 25°N section and by the corresponding temperature and tracer sea surface climatologies ('Methods'). The five sets of Green's functions provide representations of the circulation as experienced by the tracers measured during the five corresponding surveys sampled between 1992 and 2015, and thus circulation outside this sampling period is not represented ('Methods'). The MEP application assigns probability distributions on surface origins and transit times (also known as age spectrum or memory of the ocean)[32,33] since last contact with the atmosphere to each sampling point of the 25°N hydrographic surveys, modelling a water sample as the mixture of surface water masses. Relating ocean interior to surface variability overtime, the method makes it possible to decipher the ocean interior excess heat spatiotemporal origins in response to regional climate fluctuations and thus provides unprecedented documentation of ocean heat content change.

We show that redistribution of excess heat by water masses in the lower limb of the AMOC from their region of formation in the Labrador, Irminger, and Nordic Seas to the subtropical North Atlantic contributed 62% of the full water column warming at 25°N for 1850–2018, sequestering excess heat in the deep ocean and outweighing the mitigation of global warming by the upper ocean. Analysis of the decadal variability of ΔOHC at 25°N in response to regional climate fluctuations, including the NAO phase shifts, highlights distinct responses from the Nordic versus the Labrador and Irminger Seas and stresses a resilient cooling to global warming from the northeast subpolar Atlantic relative to 1850. While a lot of attention has been given in the past to the warming from the Labrador Sea Water, the contribution from the Nordic Seas now deserves special attention as we forecast that the Nordic Seas will become the prominent contributor to the deep layer warming at 25°N during the next five decades in response to the late twentieth-century warming reinforced by strong positive phases of the North Atlantic Oscillation. Finally, by computing the transport of excess heat across the section, we determine that during 2012–2018, when warming accelerates in the upper ocean, the redistribution of excess heat by the upper branch of the AMOC, attributable for 24% to southern origin excess heat, can account for the rate of warming in the domain north of 25°N. These results point out that excess heat redistribution has become a key driver of the North Atlantic heat gain.

Results

History of the 25°N warming. Figure 1b–d depicts the long-term (2018–1850) and full-depth warming along the 25°N section. The highest values, up to 0.8 °C, are in the upper subtropical gyre, a hot spot of excess heat storage[34–36] encompassing the upper branch of the AMOC. Below, the imprint of the AMOC lower limb stands out with the sequestration of excess heat enhanced in the deep western boundary current. It carries the ΔT of the North Atlantic deep water identified as two relative maxima up to 0.25 °C at 1500 m and 2500–3500 m. Minimum ΔT (<0.1 °C) at 800–1000 m and below 4000 m are influenced by intermediate and bottom waters from the Southern Ocean.

The reconstructed ΔT and corresponding ΔOHC time series are synthetised in Fig. 2 for four depth layers as zonal averages of the section from the Florida Strait to Africa (Fig. 1) after the Green's functions have been further constrained by a Bayesian adjustment to observations ('Methods' and Supplementary Fig. 2). The small ΔOHC observed at the beginning of our time series is attributed to the long pivotal period with no climate trend situated after the end of the Little Ice Age (Fig. 2a) and before the onset of the modern period of increasing anthropogenic forcing of global mean surface temperature[37,38]. Then the different depth layers deviate from this plateau. For the 0–700 m layer, where rapid (~5 years, Supplementary Fig. 3) ocean response to SST change occurs, ΔT evolution broadly reflects the North Atlantic SST (Fig. 2a, c) showing a prevalence of the Atlantic Multidecadal Oscillation until the 1970s, after which the accelerating greenhouse warming dominates[39]. The main ΔT trends of the layer can be directly associated with the main climate fluctuations. After a slight recovery from the little ice age cooling, the severe late-nineteenth-century cooling stands out (Fig. 2c, ΔT least-squares

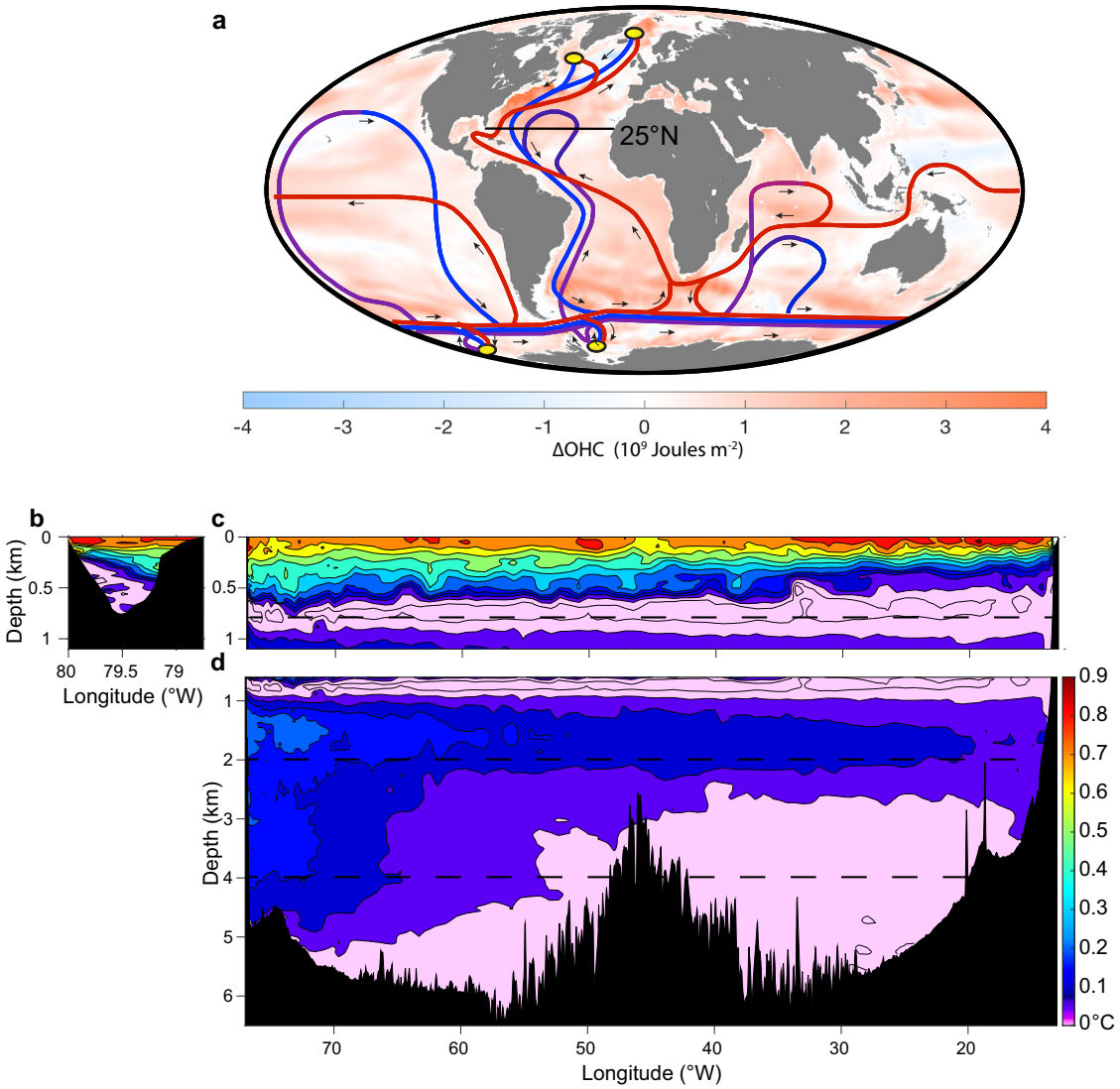

Fig. 1 Area of study and section of potential temperature anomaly in 2018 relative to 1850. a Location of the A05 basin-wide hydrographic section along 25°N (black line) superimposed on the spatial map of annual mean 0–2000 m ΔOHC (10^9 Joules m^{-2}) in 2019 relative to a 1981–2010 baseline (IAP data[7, 87]). The schematic of the meridional overturning circulation (MOC) shows surface currents carrying heat towards the poles (red line) and the North Atlantic Deep Water and Antarctic Bottom Water formation sites (yellow dots) where surface waters lose buoyancy, downwell, and subsequently feed the deep (blue) and bottom (purple) return flows of the MOC, adapted from ref. [88]. **b**–**d** Vertical distribution of reconstructed potential temperature anomalies (°C) in 2018 relative to 1850 along A05 for (**b**) the Florida Strait, (**c**) the top 1100 m and (**d**) below 1000 m of the transatlantic section. The colour scale in (**d**) applies also to (**b**) and (**c**). The dashed lines delimit the depth layers used for the section averages.

trend of −0.085 ± 0.012 °C/decade during 1879–1919). Then, two main periods of warming are observed during the twentieth century: the early-twentieth-century warming (0.068 ± 0.015 °C/decade during 1923–1959, 0.1 ± 0.02 during fast phase 1923–1943) and the late-twentieth-century warming (0.078 ± 0.008 °C/decade, 1975–2007) interrupted by the mid-twentieth-century cooling (−0.138 ± 0.023 °C/decade, 1959–1975). During the early-twenty-first century, a warming acceleration (0.22 ± 0.011 °C/decade) is noticed after a slight 2007–2012 slow-down (0.02 ± 0.023 °C/decade). Below 700 m, the signals are lagged by the longer timescales for transport from the surface source regions to the 25°N section and attenuated by mixing along their paths. For 700–2000 m (Fig. 2d), after initial warming (0.011 ± 0.005 °C/decade), the ΔT time series show two cooling-to-warming reversals: from 1939 an 18 years of cooling (−0.051 ± 004 °C/decade) switching in 1957 to a long warming (0.038 ± 0.002 °C/decade) and from 1997, an intense but brief cooling (−0.127 ± 0.005 °C/decade) switching in 2005 to a warming (0.061 ± 0.005 °C/decade). The 2000–4000 m ΔT evolution (Fig. 2e) is dominated by long-term warming from 1940 to 1997 (0.011 ± 0.001 °C/decade) followed by a short 8 years of cooling in 1997–2005 (−0.012 ± 0.001 °C/decade) returning to warming in 2005 (0.012 ± 0.001 °C/decade). The abyssal layer (Fig. 2f) shows a ΔT pattern comparable to that of the 2000-4000 m layer. The trends in the upper ocean mirror the major climate fluctuations in the North Atlantic, and in the lower ocean, signals are of much lower frequency but still show strong variability, the origin of which will be deciphered below in this paper.

Our time series agree well with the observation-based ocean reanalyses (ORAs) EN4, IAP and ISHII for the upper layer from 1975 (best-sampled time period considered the most reliable, Fig. 2c) and to a lesser extent for the intermediate layer (Fig. 2d).

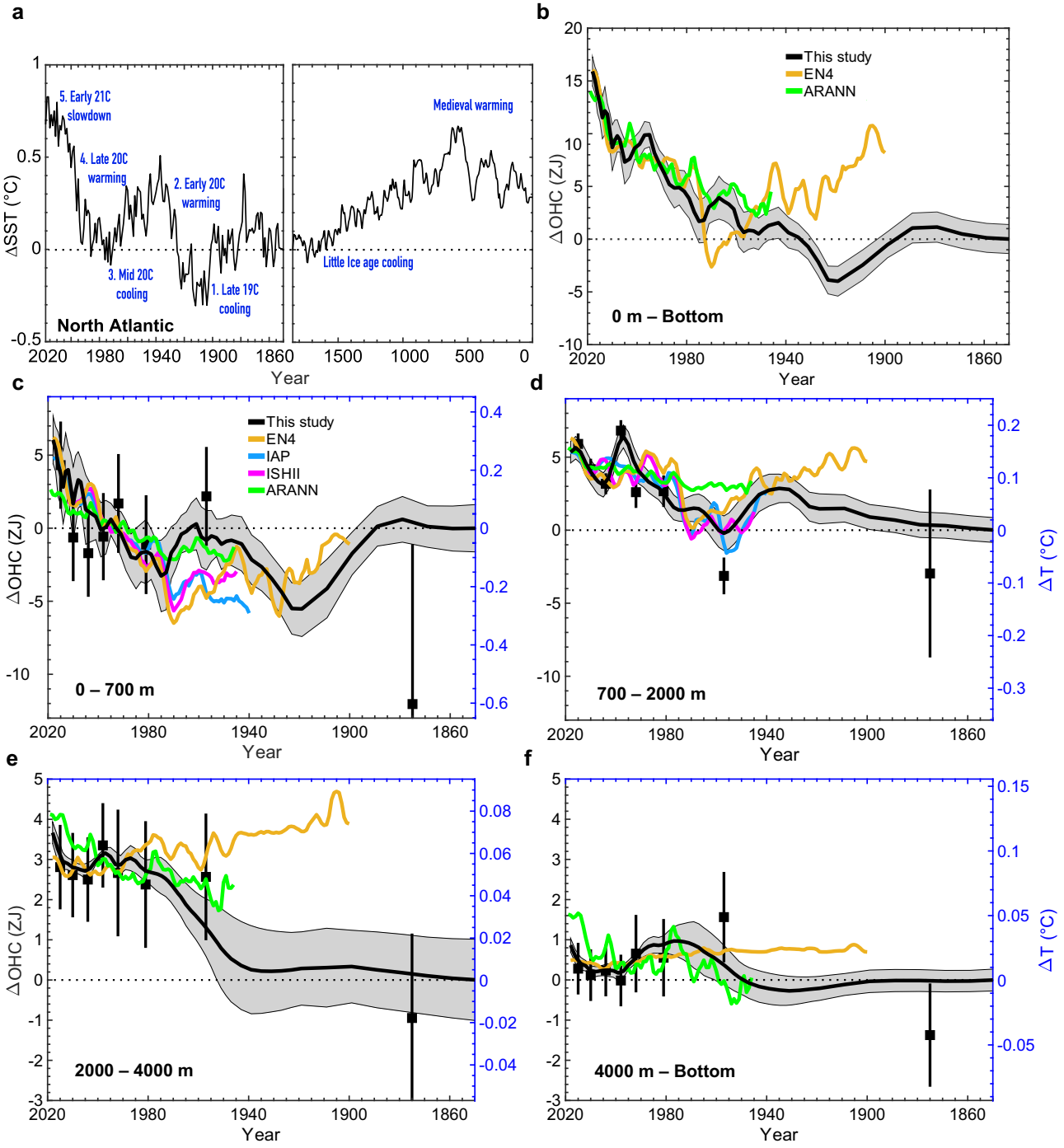

Fig. 2 Reconstructions of temperature and OHC changes at 25°N with comparison to hydrographic surveys and reanalyses. a Time series of North Atlantic (0–89°N) ERSSTv5 ΔSST (left panel) for years 1854 to present and of global mean ΔSST EQ-0015[15] (right panel) for years 0 to 1854 (see Data). Recent climate periods are adapted from Yao et al.[89]. **b**–**f** Time series of zonally and vertically averaged temperature anomaly (ΔT in °C, right *y*-axis) and section-integrated ocean heat content anomaly (ΔOHC in ZJ = 10^{21} J, left *y*-axis) for our reconstruction (black) and ocean reanalyses (ORAs; EN4 (orange), IAP (cyan), ISHII (magenta) and ARANN (green), see Data). **b** shows the full water column (ΔOHC only) and the four depth ranges are displayed in (**c**) top 700 m, (**d**) 700–2000 m, **e** 2000–4000 m, (**f**) 4000 m–bottom. ORAs are the mean for the 20°N–30°N latitude band, and for comparison, our ΔOHC reconstructions at 25°N are extrapolated in latitude by 10 degrees to cover the band 20°N–30°N. The ORAs are referenced to our 1981–2010 baseline mean. The grey shading shows the one standard deviation of the temperature estimated from the 5005-member ensemble computed using the five different cruises and 1001 different SSTs ('Methods'). The squares with error bars are the hydrography-based values corrected for the different cruise tracks (Supplementary Note 1).

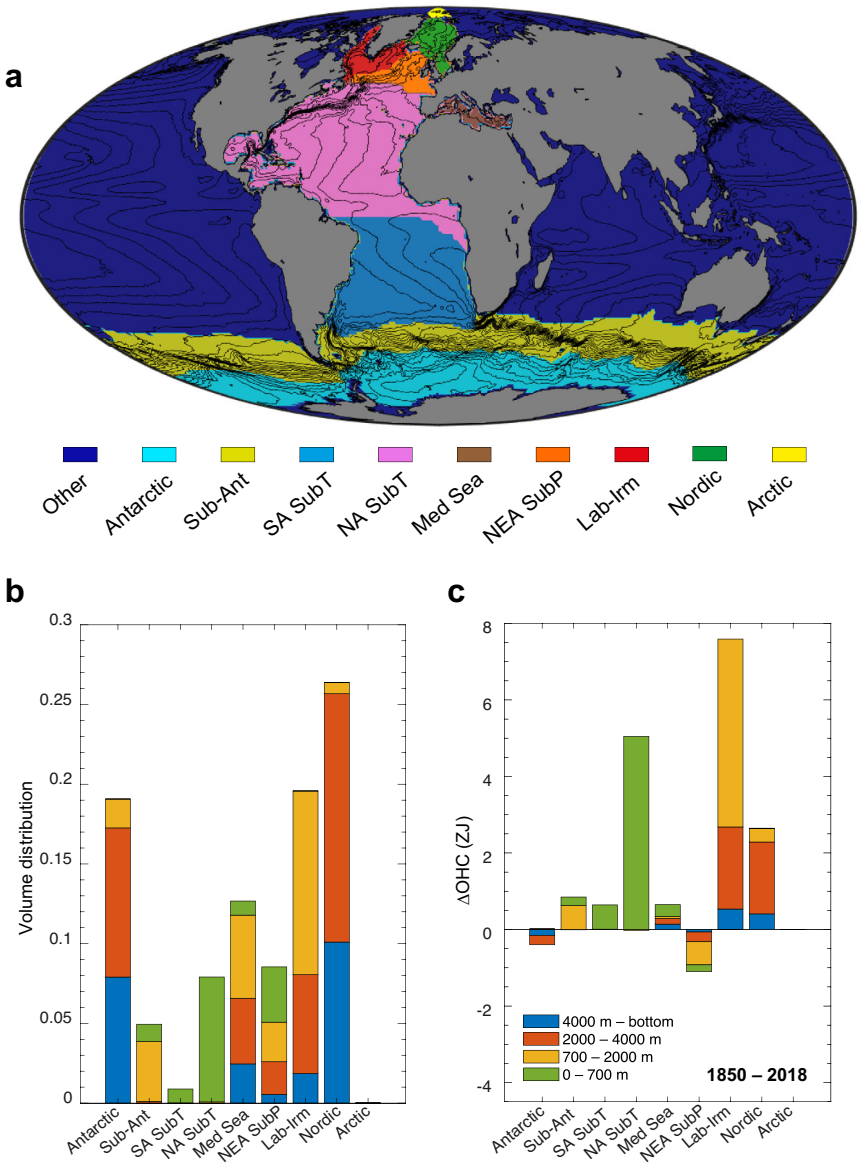

Fig. 3 Source regions and their contributions to volume and ΔOHC at 25°N in 2018. a Map of the main source regions, superimposed on the mean ocean dynamic topography, which displays the main features of the ocean steady-state circulation. Colours delimit the different regions as indicated on the panel. The nine source regions are the western Eurasia Basin (Arctic), the Nordic Seas (Nordic), the Labrador and Irminger Seas (Lab-Irm), the north-eastern subpolar Atlantic (NEA SubP), the Mediterranean Sea (Med Sea), the tropical and subtropical North Atlantic (NA SubT), the tropical and subtropical South Atlantic (SA SubT), the Sub-Antarctic (Sub-Ant) and the Antarctic (Supplementary Note 2). There are no contributions from region Other ('Methods'). **b** Regional contributions to the volume at 25°N from the regions indicated in map a. Colours refer to different depth ranges: 0–700 m (green), 700–2000 m (yellow), 2000–4000 m (red), 4000–bottom (blue). Volumes are normalised to the total volume = 1. **c** same as (**b**) but for ΔOHC (ZJ) in 2018 relative to 1850. The regional contributions were obtained by summing over all patches of our 5° × 5° gridded world ocean belonging to each of the regions ('Methods' and Supplementary Fig. 4).

Before 1975, our reconstruction and that of Bagnell and DeVries[17] show the early-twentieth-century warming in the upper layer extending to 1960 whereas it stops earlier in EN4 in favour of the subsequent cooling (Fig. 2a, b). The substantial warming of the 700–2000 m layer seen in our reconstruction from the late 1950s (Fig. 2d) has been largely reported in the literature[14,40–42] and is also evidenced in ORAs. Furthermore, the noticeable cooling-to-warming sequence between 1940 and 1990 is also seen in EN4 and IAP. For the 2000–4000 m layer, our reconstruction shows steep warming between 1945 and 1980, also seen in Gebbie et al.[15] (their Fig. 3) and hinted by Bagnell and DeVries[17]. Below 4000 m, EN4 does not reproduce the 1945–1980 warming seen in our reconstructions, in Bagnell and DeVries[17] and Gebbie et al.[15] (their Fig. 3). However, EN4 shows some consistency with the recent cooling-to-warming reversal highlighted by our time series and also seen in decadal surveys[43] and in Bagnell and DeVries[17]. The discrepancy between our results and EN4 is the largest in the deep ocean before 1960 when there is sparse observation coverage[44]. Our comparison to the independent 1873–76 Challenger temperatures shows a good agreement except in the upper ocean where Challenger temperatures also diverge from SST anomalies for this period (Fig. 2c, a). Summing up, our reconstruction of ΔOHC for the full depth ocean (Fig. 2b) shows warming from the 1930s that agrees

well with Bagnell and DeVries unabated warming from 1946. This contrasts with the 1940–70 pronounced cooling found in EN4 full-depth ocean for which warming starts in 1970.

Our resulting warming between 1850 and 2018 is 0.304 °C ± 0.08 for the 0–700 m and is 0.075 °C ± 0.05 below 700 m, thus four times smaller than the upper layer. However, considering their large volumes, the layers below 700 m account for 62% of the full water column ΔOHC (6 ± 1.6 ZJ in the upper ocean and 9.9 ± 1.4 ZJ below). The heat gain partitioning is 33.6% for 700–2000 m (5.3 ± 1.0 ZJ), 23% for 2000–4000 m (3.7 ± 0.6 ZJ) and 5.4% for 4000 m–bottom (0.9 ± 0.3 ZJ). Those findings are compatible with the reconstruction of the Atlantic Ocean by Gebbie et al. (their Fig. 5)[15] suggesting that 53% (19%) of the warming since 1850 occurred below 700 (2000) m, but not with the lower contributions of the deep ocean of Zanna et al.[16] (23% and 4%, their Fig. 1; note that Zanna et al.[16] neither considered the Nordic Seas as a source region nor the SSTs before 1854). The Bagnell and DeVries[17] ΔOHC reconstruction for 1946–2017 at 25°N in the Atlantic Ocean shows a warming distribution of 43% for 0–700 m, 24% for 700–2000 m and 33% below, comparable to the 40, 30 and 30%, respectively, found for our reconstruction for the same period. Those reconstructions highlight the important role of the deep waters in sequestering heat.

Origin of excess heat. To explain the ΔOHC evolution at 25°N, we first determine the surface source regions that feed the water masses of the section and quantify their contributions to warming for 2018 relative to 1850. Figure 3 shows the origin of ΔOHC at 25°N as the contributions from nine source regions (also qualified as uptake regions). The North Atlantic contributes to 93% (14.8 ± 1.9 ZJ) of the warming at 25°N, although its regions only supply 75% of the water masses at 25°N, the rest of the water mass volume being ventilated in the Southern Hemisphere (Fig. 3b). The tropical and subtropical North Atlantic (NA SubT, 5.0 ± 1.2 ZJ) warm the upper layer by 81%. Below, the main northern contributors are the Labrador and Irminger Seas (Lab-Irm, 7.6 ± 1.0 ZJ) and the Nordic Seas (Nordic, 2.6 ± 0.9 ZJ) respectively warming the intermediate layers by 82.3% and 6%. Although Lab-Irm contributes less to the volumes of the deep (15.8%) and bottom layers (8.9%), it warms these layers more (51.4%, 49.4%) than Nordic (45%, 37.7%). The Mediterranean Sea warms all layers by less than 4% (0.7 ± 0.4 ZJ), despite a large volume contribution (13%). In regard to the negligible contribution from the Arctic, note that we are considering only the western Eurasia Basin (Fig. 2 and Supplementary Note 2). That said, it is likely that some Arctic contribution is counted as Nordic and Lab-Irm because Arctic waters flow southward through Fram Strait in the shallow East Greenland Current towards Nordic and Lab-Irm before subducting. The southern hemisphere accounts for less than 7% of the warming (1.1 ± 0.4 ZJ). This contribution is from the Sub-Antarctic (0.8 ± 0.2 ZJ, warming the intermediate layer by 10.5%) and tropical and subtropical South Atlantic (SA SubT, 0.6 ± 0.3 ZJ, 10.2% of the upper layer warming). Interestingly, although all the layers show net warming, the north-eastern subpolar Atlantic (NEA SubP, −1.1 ± 0.3 ZJ) cools the upper (−0.2 ± 0.2 ZJ), intermediate (−0.7 ± 0.1 ZJ) and deep (−0.2 ± 0.3 ZJ) layers while the Antarctic (−0.4 ± 0.4 ZJ) cools the deep (−0.2 ± 0.3 ZJ) and abyssal (−0.2 ± 0.2 ZJ) layers. Overall, the most striking result is the prevalent warming in the North Atlantic deep water, surpassing that of the NA SubT in the upper ocean. Its surface origins are mostly from the Lab-Irm but also from the Nordic Seas whose substantial contribution is, to the best of our knowledge, identified here for the first time.

Interdecadal changes in regional contributions and projections. Turning our attention to the regional climate fluctuations in the source regions and how they impact decadal heat content change at 25°N overtime, we show in Fig. 4 the SST anomalies (ΔSST) times series in the source regions for the largest contributors and the ΔOHC responses at 25°N. First, we analyse the ΔSST times series. The signatures of the main climate periods identified by numbers 1–6 in Fig. 4 are readily seen on the regional ΔSSTs albeit modified by the interplay with North Atlantic Oscillation (NAO)[45,46]. NEA SubP and Lab-Irm SSTs show cooling during NAO-positive phases (NAO+, e.g., 1900–22, 1972–95, also periods of enhanced convection) and, in opposition, Nordic SST experiences warming during those NAO+ periods and cooling during NAO− (1955–1971, Fig. 4a, b, f)[47–49], consistent with Deser et al.[48]. NAO changing phases are thus seen enhancing or counteracting the main climate fluctuations in ΔSST as further discussed below (Fig. 4a, c, d). Because Green's functions allow us to calculate the impact at 25°N of SST variability of each 5° × 5° patch, they are unique tools to identify how these superimposed signals propagate and when these signals reach 25°N. This is evidenced in Fig. 4b–f showing that ΔOHC time series at 25°N bears a strong resemblance to the corresponding uptake region ΔSST time series with a lag equivalent to the modal age of the transit time distribution (see also Supplementary Fig. 3). Those modal ages range from 0 to 5 years in the SA SubT and NA SubT, 10 years in the NEA SubP to 40–55 years for regions contributing below 700 m (Lab-Irm, Nordic, Antarctic, Sub-Ant, Med-Sea). The correspondence is not one to one however as the Green's Function age spectrum, which characterises the cumulative ventilation, is far more complex than a single time scale[50] (Supplementary Fig. 3) due for example to the multiplicity of pathways between the source regions and 25°N (rapid propagation within the deep western boundary current[46,51], slower interior routes and recirculations, mixing). Still, the low-frequency variability of ΔSST being preserved during propagation, insights on how and when regional climate fluctuations impact ΔOHC decadal variability at 25°N can be drawn from Fig. 4 and quantified hand in hand with a detailed view of the source region contributions to the different depth layers (Fig. 5).

Figure 5 highlights NA SubT and Lab-Irm as the main contributors to the 25°N OHC variability. The NA SubT sets the upper ocean ΔOHC; its contributions cancel out over the 1850–1997 period after which NA SubT builds up the layer warming (4.3 ± 1.5 ZJ) augmented by NEA SubP (1.1 ± 0.3 ZJ). The overall NEA SubP contribution is, however, negative in response to ΔSST that remained mostly negative since 1850 (Fig. 4b). Lab-Irm sets the intermediate layer ΔOHC with clear signatures of both the NAO phases and the main climate fluctuations but overall shows a warming accumulation in response to the continuously positive ΔSST since 1850 (Fig. 4c). As the upper ocean cools (−5.7 ± 0.7 ZJ) between 1850 and 1923 (Fig. 5a), the intermediate layer at 25°N shows a heat gain coming from warming in Lab-Irm (2.6 ± 0.7 ZJ) moderated by cooling in Med-Sea (−0.8 ± 0.5 ZJ). Then, between 1923 and 1959 (Fig. 5b), the intermediate layer shows a modest heat loss (−1.4 ± 0.5 ZJ) from all its contributors which we attribute to the predominance of the late-nineteen-century cooling and a switch to NAO+. The high heat gain between 1959 and 1997 (Fig. 5c, d) builds up from Med-Sea (1.0 ± 0.4 ZJ) and Lab-Irm (5.4 ± 0.7 ZJ) from the lagged response to the early-twentieth-century warming delayed until 1975 in Lab-Irm by NAO+ (Fig. 4c, f). The reversal to an intense heat loss (−3.5 ± 0.6 ZJ) between 1997 and 2005 (Fig. 5e) is attributed to the superimposition of Lab-Irm deep winter convection (1950–1955)[52] with the mid-twentieth-century cooling (Fig. 4c). Heat gain (2.2 ± 0.6 ZJ) at 25°N resumes between 2005 and 2018 (Fig. 5f) mainly from the interruption of the mid-twentieth-century cooling in Lab-Irm and the shutdown of deep

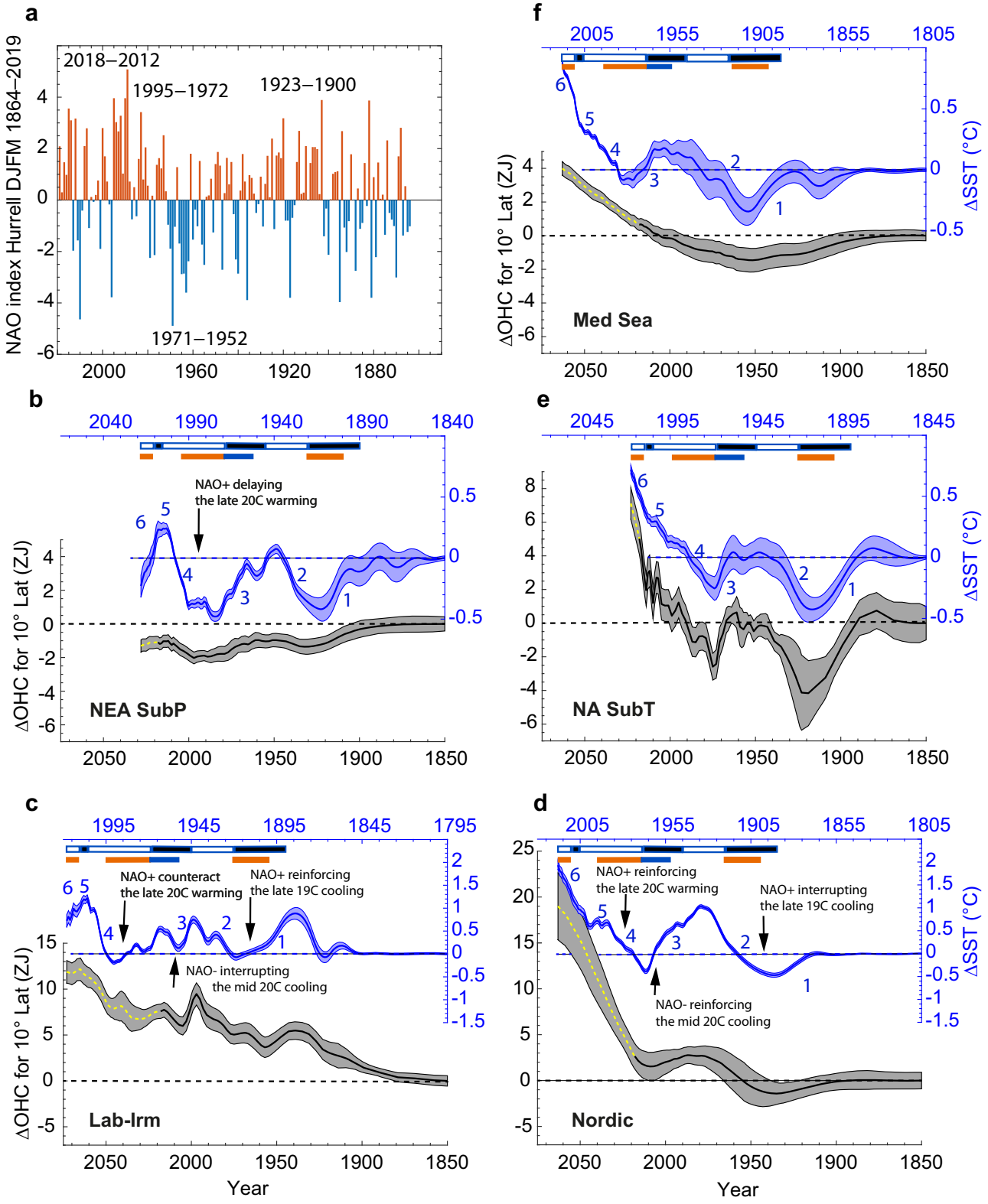

convection under NAO−[53] (1955–1971, Fig. 4a, c). Because of the lagged response of the deep ocean to surface conditions, the Green's Function framework also provides a new forecasting tool for deep OHC change on time scales of the modal ages, assuming no change in the circulation which is constrained here by the five 1992–2016 hydrographic surveys ('Methods'). From 2018, Fig. 4c forecasts a slight decrease in OHC at 25°N, echoing the 1965–1975 SST cooling in Lab-Irm. It is followed by modest changes as the 1975–1995 NAO+ counteracts the late-twentieth-century warming. The latter then drives a substantial OHC increase (4 ± 0.8 ZJ) between 2045 and 2060 interrupted by a slight reversal in response to the recent 2006–2018 SST cooling period. Although those cooling events have produced replenishments of convected water under NAO+[52,54], the latter vintage

Fig. 4 Historical contributions of the North Atlantic source regions to full water column ΔOHC at 25°N and their future projections. a Time series of NAO index[45]. **b** Times series of the ΔSST (blue, right *y*-axis) and of the full depth ΔOHC response at 25°N (black, left *y*-axis), both relative to 1850, for the NEA SubP source region defined in Fig. 3a. The ΔOHC is extrapolated in latitude over 10 degrees as in Fig. 2. The ΔSST are regionally averaged over 5° × 5° patches, each patch being weighted by its contribution to the full water column at 25°N. The ΔSST are low-passed filtered using a 10-year moving mean. The ΔSST time axis is shifted backward in time by the modal age to highlight the correspondence between ΔSST and ΔOHC. The Green's functions potential to infer the interior signal from past ΔSST is also used to project ΔOHC in the future over a time span equal to the modal age (yellow dotted line). The grey shading represents the one standard deviation of the time series estimated as in Fig. 2. **c**–**f**. Same as for (**b**) but for Lab-Irm, Nordic, NA SubT, Med-Sea. Note the different *y*-axis scales. The six climatic epochs identified in Fig. 2a are indicated by numbers as follows: **1**. Late-nineteenth-century cooling (1879–1919), **2**. Early-twentieth-century warming (1923–1943), **3**. Mid-twentieth-century cooling, (1943–1970), **4**. Late-twentieth-century warming (1975–2007), **5**. Early-twenty-first-century slowdown (2007–2012), and **6**. Early-twenty-first-century acceleration (2012–2018). Horizontal bars indicate NAO+ (orange), NAO− (blue) when it lasted for more than 5 consecutive years, and cooling (black) and warming (white) corresponding to the six climatic epochs.

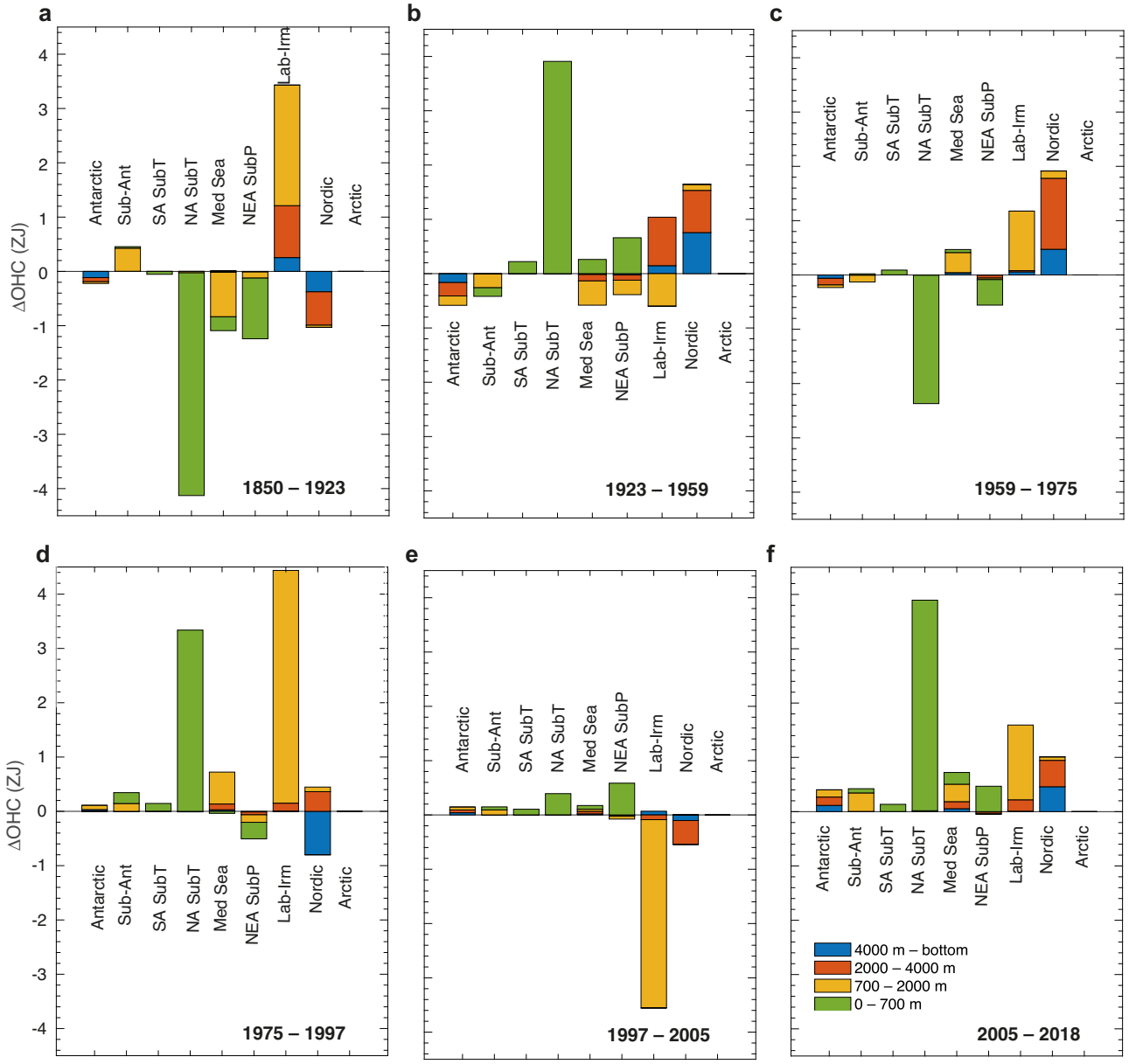

Fig. 5 Regional heat uptake contributions to 25°N ΔOHC for six time intervals. Same as Fig. 3 but for excess heat contributions (ZJ) from the source regions for different time intervals at 25°N, which we observed, have shaped the 0–700 m ΔOHC: (**a**) 1850–1923, (**b**) 1923–1959, (**c**) 1959–1975 (**d**) 1975–1997, (**e**) 1997–2005, and (**f**) 2005–2018.

was warmer than the vintage of the early 1990s suggesting that it has sequestered anthropogenic warming (Fig. 4c). Our results clearly forecast a continuity of the century-scale warming for waters coming from Lab-Irm, Med Sea and Sub-Ant (the latter plateauing around 2035, Fig. 4c, f and Supplementary Fig. 5h) and thus for the 700–2000 m layer.

The ΔOHC of the 2000–4000 m layer is mainly influenced by the contribution of Lab-Irm and Nordic, the latter displaying low-frequency intervals of ~70 years between two successive heat losses (Fig. 4d). Between 1850 and 1923 (Fig. 5a), ΔOHC shows a slight heat gain coming from Lab-Irm warming (1.0 ± 0.5 ZJ) tempered by cooling from Nordic (−0.6 ± 0.4 ZJ). Between 1923 and 1997 (Fig. 5b–d), heat gain originates mostly from Nordic (2.4 ± 1.0 ZJ) warmed during the NAO+ that interrupted the late-nineteenth-century cooling, and then by the subsequent early-twentieth-century warming (Fig. 4d), with Lab-Irm contributing less (1.1 ± 0.4 ZJ). The 1997–2005 period (Fig. 5e) shows a heat loss, previously described[43], that comes also primarily from Nordic (−0.4 ± 0.4 ZJ) and is attributed to the lagged response to the 1950–1960[49] mid-century cooling reinforced by NAO- (Fig. 4d). It reverts to warming for 2005–2018 (Fig. 5d, 0.8 ± 0.4 ZJ). The abyssal layer shows a comparable ΔOHC pattern but for an earlier and stronger occurrence of the recent shift to a cooling (1987, Fig. 2 and Supplementary Fig. 6) from Nordic (−0.9 ± 0.4 ZJ between 1975 and 2005) while Antarctic contributes to modest warming from 1975 (0.2 ± 0.2 ZJ). Finally, Fig. 4b forecasts an acceleration of Nordic contribution to the deep and abyssal warming at 25°N in response to the late-twentieth-century warming since 1970. This would make them the dominant contribution to heat gain below 700 m. We estimate that Nordic will contribute to a warming of 16 ZJ (~0.3 °C) at 25°N over 2018–2065 so 4 times the warming from Lab-Irm.

Nordic and Lab-Irm show very different responses at 25°N due in part to the opposing influence of the NAO on these two regions of North Atlantic deep water formation. Thus, during 1850–2018, deep water warming was dominated by Lab-Irm, which experienced an interruption of mid-century cooling by the 1960–1970 NAO- while Nordic had an enhancement of cooling. Also, Lab-Irm showed warming SST during 1865–1890 while Nordic SST was cooling, an opposition likely due to NAO- conditions (Fig. 4a, c and refs. [55,56]). The roles will be reversed in the next 5 decades because Lab-Irm warming has been mitigated by successive NAO+ during 1971–1995 and 2012–2018 while Nordic has experienced enhanced warming by these NAO+ and horizontal heat transport increase from the ocean[25,57].

The predominance of the warming of the full water column by the layers below 700 m was noted for the 1850–2018 long time scales (Fig. 3). The analysis of the interdecadal ΔOHC variability shows that the intermediate and deep waters at 25°N responded in the last decades to the mid-twentieth-century cooling (Fig. 4). As a result, and in opposition to 1850–2018, the strong full-depth warming for 1975–2018 (14.2 ± 1.9 ZJ, Fig. 2 and Supplementary Fig. 7) is predominantly due to the rapid response of the upper ocean[39] (9.3 ± 1.6 ZJ or 65%) to the late-twentieth-century warming and twenty-first-century acceleration while the contribution of the deeper waters is lower. Our study forecasts an important heat gain in the deep ocean of the Subtropical North Atlantic in the next 50 years as it will carry the impact of the late-twentieth-century warming as well as a modest but increasing warming from the Southern Ocean (Supplementary Fig. 5).

Where does the 25°N excess heat go? Having identified the source regions of the 25°N excess heat, we now determine how the inferred excess heat is redistributed towards the north and south of the section. Figure 6 shows the excess heat transport time series across 25°N relative to its 1975–1986 mean (ΔXHT, 'Methods'). This analysis was limited to times when we had information on the circulation strength and climatologies concord. ΔXHT time series were estimated for each of the 1992–2015 surveys and are driven by the temperature change only (each ΔXHT time series was determined using the ΔT times series and the velocity field at the time of the survey, 'Methods'). ΔXHT five-survey standard deviation however includes variability due to circulation changes between the revisits of the section ('Methods'). For 2018, the five-survey net transport average is 19.0 ± 3.5 TW northward, liable at 86% to the AMOC (Fig. 6a). The upper (lower) limb of the AMOC carries excess heat northward (southward). Above 1000 m, in the AMOC upper limb, the northward ΔXHT amounts to 22.9 ± 7.5 TW. Below 1000 m, 3.9 ± 1.1 TW of excess heat are carried southward (Fig. 6c) mainly in the deep western boundary current where higher excess heat correlates with higher southward velocity.

The northward transport of ΔXHT across 25°N supplies heat to the north of the section at a rate that is compared in Fig. 6a to the rate of change of OHC between 25°N and the Bering Strait ($\frac{\partial OHC}{\partial t}|_{>25N}$), the latter integrating the oceanic response to all drivers. The AMOC strength variability is known to modulate the heat content of the North Atlantic[58], with a weaker (stronger) AMOC carrying less (more) heat northwards. Accordingly, $\frac{\partial OHC}{\partial t}|_{>25N}$ increases by ~1 W m^{-2} abruptly in 1990 following an AMOC[59] strengthening and drops back by ~1 W m^{-2} in 2009 as the AMOC returns to a weaker state[59,60] (Fig. 6a, b). During this period the northward ΔXHT increased due to the continuous warming of the upper layer. The difference between the ΔXHT and the warming north of 25°N can be attributed to the impact of the AMOC strengthening resulting in a larger transport of warm water northward during 1990–2009. For 2012–2018, which was under a weak AMOC, the net northward ΔXHT accumulates excess heat north of the 25°N section at an average rate of 0.89 ± 0.19 W m^{-2}, equivalent to the 0.82 W m^{-2} estimated for $\frac{\partial OHC}{\partial t}|_{>25N}$, revealing a substantial role of ΔXHT to the warming of the North Atlantic. Noteworthy, 24% of this ΔXHT comes from the southern hemisphere (SA SubT, Sub-Ant, Antarctic, Supplementary Fig. 8). Overall, the excess heat redistribution contributes to a North Atlantic warming similar to ocean global warming of 0.65 ± 0.11 W m^{-2} reported for 2006–2015 from observations[9,61] (here we have 0.67 ± 0.19 W m^{-2} for 2006–2015).

The AMOC lower limb (Fig. 6b) is found to warm the deep world ocean at a rate of 0.011 ± 0.004 W m^{-2} (2011–2018). Below 2000m, the warming rate of 0.009 ± 0.003 W m^{-2}, which is smaller than the average warming of the global ocean below 2000 m depth (0.06 ± 0.03 W m^{-2} for 1992–2011[13,61]). This evidences a contribution of the northern hemisphere to long-term storage of heat in the deep world ocean with a temporary low rate, which is explained by the recent impact of the mid-twentieth-century cooling from the Nordic, Labrador and Irminger Seas.

Discussion

As GHGs are warming the planet, how is the vast surface uptake of excess heat by the oceans redistributed in the ocean interior? To dredge into this question, we determined Green's functions to relate sea surface temperature variability of the world ocean to full depth sub-surface temperature at 25°N in the Subtropical Atlantic since the beginning of the industrial era. Our new historical reconstructions of heat content at 25°N are broadly consistent with prior studies with uncertainties expected to decrease as SST reconstructions continue to improve. Our reconstruction shows a fairly coherent view of the excess heat uptake and redistribution in regard to regional climate fluctuation. In particular, we identify

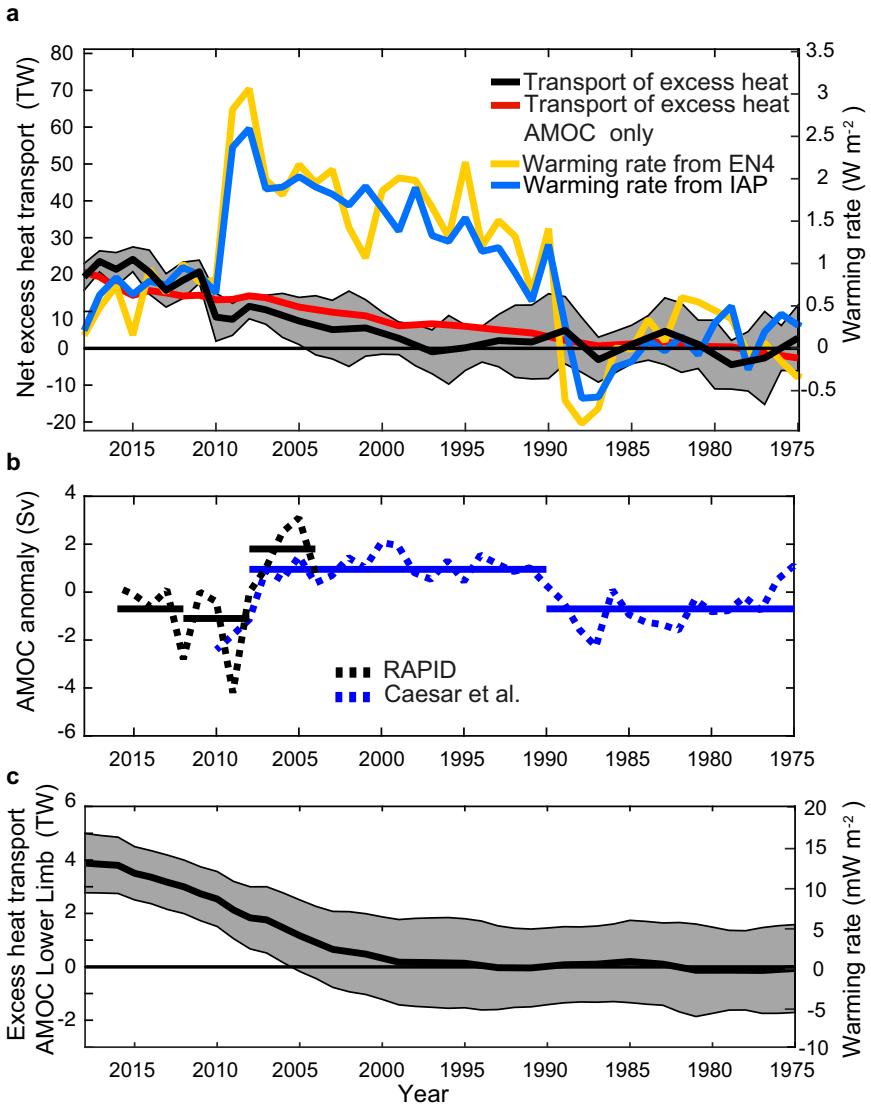

Fig. 6 Excess heat transport at 25°N and North Atlantic heat storage rates from climatologies. a Times series of ΔXHT (TW) due to the temperature-driven net transport of excess heat across 25°N (black line, positive northward). ΔXHT is also expressed as the equivalent heat flux per unit area for the region north of 25°N (W m^{-2}) and compared to the warming rate of the full-depth ocean heat content ($\frac{\partial OHC}{\partial t}|_{>25N}$) over the domain between the north of 25°N and Bering Strait (yellow = EN4 full depth, blue = IAP 0–2000 m completed by EN4 below). **b** Time series of the AMOC anomaly for 1975–2016, reproduced from Caesar et al.[90] (blue), and for 2004–2017, estimated by the in situ RAPID monitoring[60]. Caesar et al.'s time series is shifted by 5 years to account for the delayed response of Subpolar SST to AMOC variability at 25°N[91]. This shift realigns Caesar et al.'s time series with the 2009 AMOC drop observed at RAPID. The thick continuous lines show the mean values for different time periods identified as relevant to AMOC state changes. **c** Times series of ΔXHT due to the temperature-driven transport in the AMOC lower limb (depth >1000 m, positive southward), also shown as warming rate (mW m^{-2}) when applied over the world ocean surface area at 1000 m, excluding the Atlantic sector north of 25°N. Both ΔXHT time series are relative to 1975–1986 mean. The grey shading in (**a**) and (**c**) shows the one standard deviation of ΔXHT estimated from the 5005-member ensemble computed using the five different cruises and 1001 different SSTs ('Methods').

the response to the North Atlantic Oscillation as key to explain some of the differences between the variability of deep and intermediate layer heat contents captured at 25°N in decadal surveys. Over 1850–2018, the reconstruction for the waters below 700 m evidences crucial warming contributions from the Labrador (dominant) and Nordic Seas. Recently, those seas have cooled the deep subtropical North Atlantic in response to the mid-twenty-century cooling before reversing to warming. Our work suggests that the deep subtropical North Atlantic will continue in the future its overall warming as a delayed response to the warming of the Nordic Seas since 1970 and Lab-Irm since the 1990s, alongside the Antarctic Bottom Water warming trend since the 1990s (Fig. 4c, d and Supplementary Fig. 5i) and thus stresses the importance of deep waters for Earth energy imbalance and sea-level rise predictions.

The warming north of 25°N by the northward transport of excess heat is consistent with observations for the Mediterranean Arctic[25] and with models[22] that showed northward redistribution of excess heat in the Atlantic. Our study evidences a crucial role of excess heat transport for the heat balance north of 25°N and identifies the AMOC as a primary mechanism for redistributing the excess heat. Noteworthy, we obtained a 24% contribution from the southern hemisphere to the northward transport of excess heat that counteracts the hemispheric asymmetry of Atlantic air-sea excess heat uptake. We estimated that the AMOC carried a continuously increasing net northward transport of

excess heat since 1997 relative to 1975–1986 before reaching a plateau ~19 TW of excess heat transport in 2012–2018 that remarkably equals the heat content change north of the section up to the Bering Strait. We speculate that some of the northward transport of excess heat will contribute to accelerate the warming of the Arctic Mediterranean Seas and melt of sea ice.

Methods

Data. The ocean interior observations are eight snapshots of the circulation spread over 145 years. They are the 1870s HMS Challenger expedition and the seven repeat hydrographic surveys performed between 1957 and 2015 along the 25°N World Ocean Circulation Experiment (WOCE) A05 section, although they did not all follow exactly the same track and did not all measure all the tracers of interest (Supplementary Table 1 and Fig. 1). The spatially sparse depth and temperature measurements from the 1870s are taken from Gebbie[15]. Temperature, salinity and pressure data were collected for the seven A05 hydrography surveys. The water samples were analysed for geochemical tracers—dissolved oxygen (O_2), nitrate (NO_3), phosphate (PO_4), dichlorodifluoromethane (CFC-12), trichlorofluoromethane (CFC-11)—for 1992, 1998, 2004, 2010 and 2015. Sulfur hexafluoride (SF_6) was analysed in 2010 and 2015. The background ΔC14 data were interpolated from the Global Ocean Data Analysis Project (Glodap) gridded data set[62] onto the 25°N survey locations. For the determination of the Green's functions (see below), we used the last 5 surveys that have nutrient and transient tracer (CFC-12, CFC-11, SF_6 and ΔC14) data. For the Bayesian adjustment to observed temperatures (see below), we used all the surveys except the Challenger data because of the very coarse sampling of the latter (see Supplementary Fig. 1). However, we used the Challenger data as independent measurements for the comparison to our time series in the 1870s in Fig. 2.

The global surface boundary conditions cover the full world ocean and were obtained from different data sets at 1° latitude × 1° longitude spatial resolution. The O_2, PO_4 and NO_3 surface concentrations were taken from the World Ocean Atlas 2013[63] mean annual cycle. The surface background ΔC14 was taken from Glodap. In high latitudes where surface background ΔC14 is missing in Glodap, it was computed from Glodap v2[64] alkalinity using the correlation between potential alkalinity and background ΔC14 following Rubin and Key[65]. The CFC-11, CFC-12 and SF_6 ocean surface concentration histories are from a mixed layer model[66] taking into account their increasing saturation overtime for 1936–2010 and extended to present using atmospheric data from the National Oceanographic and Atmospheric Administration (NOAA) Earth System Research Laboratory (ERSL) Halocarbons and other Atmospheric Trace Species (HATS) group. Sea surface salinity histories from 1900 to 2018 are from the UK MetOffice EN4 reanalysis[67]. Sea surface temperature (SST) time series are from the NOAA Extended Reconstructed Sea Surface Temperature version 5 (ERSST v5[68]). It covers 1854 to present and was extended back in time to year 0 using the EQ–0015 global SST recovered from paleoclimate data[69] to include the impact of the warm medieval period and the little ice age. We also used an ensemble of 1000 members from ERSST v4 whose spread represents the uncertainty on the SST.

We used the following gridded ocean temperature datasets for comparison to our reconstruction at 25°N: the MetOffice statistical ocean reanalysis EN4[67] (1900 to the present, monthly, surface to bottom), the objective analysis of temperature of Ishii et al.[70] (1945 to 2012, monthly, top 2000 m), the objective analysis of temperature of the Institute of Atmospheric Physics Global Ocean Temperature[26] (IAP, 1940–present, monthly, top 2000 m), and the autoregressive artificial neural network (ARANN, 1946–2019, biannual, surface to bottom) from Bagnell and DeVries[17]. For convenience, all the gridded products used in this paper are called reanalyses.

Determination of the Green's functions. We assume that tracer propagation in the ocean can be modelled by a Green's Function that relates time-and-space varying surface boundary conditions to interior tracer distributions[71]. We use the maximum entropy principle[72] (MEP), which has the ability to incorporate prior information, and observational constraints to estimate a Green's Function G for each sampling point in the ocean interior. G is a probability density function depending on transit times and surface locations (when and where the last contact of the water with the atmosphere occurred). Our set-up of the MEP follows previous work[33,73] and our notations were adapted from Holzer et al.[33], which can be referred to for further details. G has three dimensions (s: surface patches, n: years and m: months) and was estimated for transit time in the range 0–2000 years, 12 months per year and 836 patches corresponding to a division of the surface ocean into 5° latitude × 5° longitude (see Supplementary Note 3 for details of the discretization). Given the measurement $C_j^I(r_0, n_0, m_0)$ of a tracer j at location r_0 and time (n_0, m_0) in the ocean interior (I) and the surface boundary condition $C_j^{\mathrm{Surf}}(s, n, m)$ for this tracer at location and time (s, n, m), the Green's Function $\mathscr{G}(\mathrm{s, m, n}|r_0, n_0, m_0)$ relates surface boundary conditions to interior data such that

$$\mathscr{C}_j^I(r_0, n_0, m_0) = \sum_{s,m} \mathscr{G}(\mathrm{s, n, m}|r_0, n_0, m_0) * C_j^{\mathrm{Surf}}(s, n, m) \quad (1)$$

where * denotes the convolution product and $\mathscr{C}_j^I$ is an estimate of C_j^I. Given an a priori estimate $\mu(s, n, m|r_0, n_0, m_0)$ of $\mathscr{G}$ and following the MEP, $\mathscr{G}$ is uniquely defined for the maximum of

$$S = -\sum_{s,n,m} \mathscr{G} \log\left(\frac{\mathscr{G}}{\mu}\right) + \sum_{j=1}^{J} \lambda_j \left(C_j^I - \mathscr{C}_j^I(\mathscr{G})\right) \quad (2)$$

where J is the number of measured tracers and λ_j are Lagrange multipliers. $\mathscr{G}(\mathrm{s}, n, m|r_0, n_0, m_0)$ defines the probability that a mixing component at location s and a transit time (n, m) contributes to C_j^I. The cost function S combines the maximum entropy regularisation term (first term on the right-hand side) and the constraints (i.e., the differences between the estimated $\mathscr{C}_j^I$ and the measured tracer concentrations C_j^I). It permits reconstructing the observations exactly and their time histories at their sampling points. The determination of the maximum of the cost function S follows Holzer et al.[33].

We focus on the subtropical Atlantic Ocean and the five repeats of the 25°N hydrographic section where geochemical tracers were measured. We used interior observations of eight tracers and their surface boundary conditions to compute the Green's functions. The eight tracers are: potential temperature θ, practical salinity S, preformed nitrate NO_3*, preformed phosphate PO_4*, chlorofluorocarbon CFC-11, CFC-12, sulfur hexafluoride SF_6, and the prebomb ΔC14*. NO_3* and PO_4* were computed using Redfield ratio independent of the region (175:17:1 for O_2:NO_3:PO_4). Transit time distributions[71] (the time-dependant part of G) are mostly constrained by the time-evolving transient tracers CFCs, SF_6 and ΔC14*. The latter covers millennial to centennial timescales[74,75], whereas CFCs and SF_6 cover shorter time scales. For example, the CFC-12 (SF_6) atmospheric history started in the 1930s (1960s) so go back 90 (60) years only. These man-made-compounds have a fairly well-known and rapidly changing time history, providing a convincing constraint on transit time[76,77] on those shorter time scales.

The tracer surface boundary conditions were derived from the surface data sets reported above. For some data sets, the seasonal cycles were not available in the distant past. In these cases, we added to the annual value a mean seasonal cycle derived from the years of the time series for which the seasonal cycle was available. NO_3* and PO_4* were taken as cyclo-stationary following Holzer et al.[33] (mean and seasonal values are stationary and values are repeatedly cycled for each year).

The time dependency of the prior μ is given for each sampling point by the inverse Gaussian Transit Time Distribution of a 1-D advection-diffusion ocean transport model that matches the combination of the transient tracer data[78]. In our application of the Transit Time Distribution method, we adjusted the Peclet number (square ratio between the mean age and the width of the transit time distribution quantifying advection relative to mixing in the transport[79]). The location dependency of the prior μ was estimated by an Optimal Multi-Parameter[80] approach that calculates the contributions from the water mass formation area in the nine regions defined in Fig. 3 to each sampling point using corresponding surface values of the tracers.

The reconstructed time-series for tracer $\mathscr{C}_j^I(r_0, n, m)$ was computed as:

$$\mathscr{C}_j^I(r_0, n_k, m) = \sum_{s,m} \mathscr{G}(s, n, m|r_0, n_k, m) * C_j^{\mathrm{Surf}}(s, n \geq n_k, m) \quad (3)$$

where n_k is a year lag varying between present ($n_k = 0$) and 2000 years back in time. Note that although the resolution is monthly, the time series of temperature presented in Fig. 2 are annual averages. Note that we use the same $\mathscr{G}(s, n, m|r_0, n_k, m)$ for all lags n_k, which implies steady state.

The contributions of a given 5° × 5° patch s_l to $\mathscr{C}_j^I(r_0, n_k, m)$ was obtained as $\sum_m \mathscr{G}(s, n, m|r_0, n_k, m) * C_j^{\mathrm{Surf}}(s_l, n \geq n_k, m)$. The contributions of the 9 regions (Figs. 3 and 5) were obtained by summing over all patches s_l belonging to each of the regions.

Bayesian adjustment. Each set of Green's functions and corresponding potential temperature time series are specific to the survey they were inferred from and to the Green's functions time frame, 0 to the date of the survey. Nevertheless, 5 potential temperature time series inferred from the 5 surveys show much similarity (Supplementary Fig 2), giving confidence on the robustness of the methodology. Yet, the potential temperature θ time series of the depth layers reconstructed from one survey does not fully capture all the variability specific to the other 7 surveys (Supplementary Fig 2). Therefore, we further adjusted each of the 5 sets of G to the observations of the 7 surveys (1957 to 2015) to ensure that the reconstructed temperature time series be close in a least squares sense to all temperature observations, merging compatibly the information from all surveys. This was done by minimising the following cost function:

$$(\mathscr{G}_{\mathrm{bayesian}} - \mathscr{G})^2 + \alpha \sum_I \frac{\left(\theta^I\left(\mathscr{G}_{\mathrm{bayesian}}\right) - \theta^I_{\mathrm{hydrographic}}\right)^2}{(\sigma^I)^2} \quad (4)$$

where $\mathscr{G}_{\mathrm{bayesian}}$ is the adjusted Green's Function, $\theta^I\left(\mathscr{G}_{\mathrm{bayesian}}\right)$ is the potential temperature obtained by convoluting $\mathscr{G}_{\mathrm{bayesian}}$ with the SSTs, $\theta^I_{\mathrm{hydrographic}}$ are the temperature observations from the hydrographic sections, σ^I is the error associated with $\theta^I_{\mathrm{hydrographic}}$ and α is a weighting factor selected such that after minimisation the two terms of the cost function be order 1.

The σ^I are reported in Fig. 2 and include errors due to seasonal variability and to the different tracks of different cruises. Both errors were estimated by simulating each cruise in the EN4 data set and computing the deviations from the annual mean and from a reference track (see Supplementary Fig. 1). Note that, given their very coarse sampling, Challenger data were not used in the Bayesian adjustment, but were kept as independent measurements for display in Fig. 2.

Heat content was obtained by summing the temperature data multiplied by $\rho_0 C_P$ (where ρ_0 is the density of seawater, C_P is seawater heat capacity, $\rho_0 C_P = 4.1 \times 10^6\ \mathrm{J\,m^{-3}\,K^{-1}}$ was used throughout) and by the area A associated with each grid point.

Uncertainties. The errors on our potential temperature θ time series were computed as follows. First, a set of Green's functions (there is one Green's function per sampling point) was estimated for each of the 5 hydrographic surveys. Then, each of these sets of Green's functions was convoluted with the NOAA-ERSSTv5, and each of the 1000 members of the NOAA-ERSSTv4 SST ensemble (perturbations of NOAA-ERSSTv4 built so that the standard deviation of the 1000 members describe the error on the SSTs) leading to the 5005 different time series of temperature anomaly along the 25° N line. The errors are the standard deviations of these 5005 estimates. Therefore, these errors account for the standard deviations in the SST as described by the 1001 different SSTs, as well as uncertainties in tracer measurements and standard deviation due to changes in the circulation[81] as described by the 5 different sets of Green's functions derived from the 5 different hydrographic surveys (the Green's functions carry information about the transport by the circulation of the admixture components from the time they left the surface to the time of sampling.).

The Green's functions represent the circulation that has propagated the tracers measured during the five hydrographic surveys of 1992–2015. Changes in the circulation outside this sampling period are therefore not reflected in these Green's functions and the circulation used for our reconstructions is biased towards this sampling period. For the same reason, the uncertainty due to the circulation can have a similar bias. Typically, we expect 10% to 15% changes in AMOC intensity over the last millennium[82,83,84]. Noteworthy, it has been suggested that a ±25% change in the circulation, applied to the little ice age relative to the 1990s, does not affect the qualitative patterns of ΔT propagation in the North Atlantic over the common era and causes only limited changes in the signal amplitudes and times of arrivals[69] (their Fig. 3S).

Transport calculations. The absolute geostrophic velocity field perpendicular to the hydrographic survey was estimated for each of the five repeated surveys following Atkinson et al.[30]. A reference velocity was determined to reach a balance in volume transport between the Ekman transport, the Gulf Stream and interior geostrophic transports. Velocities in the bottom triangle (area below the deepest common level of the two hydrographic profiles used to compute geostrophic velocity) were computed as in Atkinson et al.[30]. The Gulf Stream and Ekman transports were from Atkinson et al.[30] except for the 2015 transports that were from Morarji[85]. Volume transports were computed by multiplying the velocities by the area associated with each grid point as for the computation of heat content, taking into account that the velocity grid is at mid-distance between two hydrographic stations. Heat transport time series across the section presented in Fig. 6 was computed by first interpolating the temperature estimates on the same vertical grid as the velocity, then converting the temperature to heat, then averaging heat at two adjacent hydrographic stations and multiplying it by the velocity and the associated area. This was done for each time step of the temperature time series and for each cruise using the velocity field derived from this cruise. The time series in Fig. 6 are the averages of the times series computed for the five repeated CTD surveys performed during 1992–2015. Their 1975–1986 mean is set at zero for reference.

Data availability

The ERSST sea surface temperature data are available from the NOAA Earth System Research Laboratory at https://www1.ncdc.noaa.gov/pub/data/cmb/ersst/. The IAP data are available from the National Oceanographic Data Cheng, Lijing & National Center for Atmospheric Research Staff (Eds) at http://159.226.119.60/cheng/ and www.mecp.org.cn/. The ISHII data are available at https://climate.mri-jma.go.jp/pub/ocean/ts/ and described in Ishii et al.[70]. The Met Office EN4 objectively analysed hydrographic data version 4.2.1, which are available from https://www.metoffice.gov.uk/hadobs/en4/. The HadiSST data are from the National Center for Atmospheric Research Staff (Eds). Last modified 27 Feb 2020. 'The Climate Data Guide: SST data: HadiSST v1.1.' Retrieved from https://climatedataguide.ucar.edu/climate-data/sst-data-hadisst-v11. The CFCs and SF_6 atmospheric data are from https://www.esrl.noaa.gov/gmd/hats/data.html. The modelled CFC-11, CFC-12 and SF_6 surface concentrations are available from http://www.apl.washington.edu/project/project.php?id=cfc_mixed_layer. The nutrients surface data are from the WORLD OCEAN ATLAS 2013 available at https://climatedataguide.ucar.edu/climate-data/world-ocean-atlas-2013-woa13. The radiocarbon data are from Glodap V1.1 available at https://cdiac.ess-dive.lbl.gov/ftp/oceans/GLODAP_bottle_files/. The bottle data are available through https://www.bodc.ac.uk, https://cchdo.ucsd.edu and https://www.nodc.noaa.gov. The reconstructed OHC time series (Figs. 2 and 4) are available from SEANOE https://doi.org/10.17882/87126. The historical (years 20 to 2015) EQ-0015 global SST, the gridded temperature anomalies and the temperature profiles of the 1870s HMS Challenger expedition from Gebbie et al.[15] are available at the National Centers for Environmental Information (NCEI, accession number 0178641). The gridded temperature field from the autoregressive artificial neural network (ARANN) method of Bagnell and DeVries[17] is from https://doi.org/10.6084/m9.figshare.12959489. The NAO index data were provided by the Climate Analysis Section[86], NCAR, Boulder, USA, Hurrell (2003). Hurrell, James & National Center for Atmospheric Research Staff (Eds). Last modified 24 Apr 2020. 'The Climate Data Guide: Hurrell North Atlantic Oscillation (NAO) Index (station-based)'. Retrieved from https://climatedataguide.ucar.edu/climate-data/hurrell-north-atlantic-oscillation-nao-index-station-based. Accessed on 06 January 2021.

Code availability

The determination of the maximum of the cost function S used the Matlab software function fsolve.

Received: 16 September 2021; Accepted: 22 April 2022;
Published online: 17 May 2022

References

1. Hansen, J. et al. Earth's energy imbalance: confirmation and implications. *Science* **308**, 1431–1435 (2005).
2. Levitus, S. et al. Anthropogenic warming of Earth's climate system. *Science* **292**, 267–270 (2001).
3. Johnson, G. C., Lyman, J. M. & Loeb, N. G. Improving estimates of Earth's energy imbalance. *Nat. Clim. Chang.* **6**, 639–640 (2016).
4. von Schuckmann, K. et al. An imperative to monitor Earth's energy imbalance. *Nat. Clim. Chang.* **6**, 138–144 (2016).
5. Trenberth, K. E., Fasullo, J. T., von Schuckmann, K. & Cheng, L. Insights into Earth's energy imbalance from multiple sources. *J. Clim* **29**, 7495–7505 (2016).
6. Levitus, S. et al. World ocean heat content and thermosteric sea level change (0–2000 m), 1955–2010. *Geophys. Res. Lett.* **39**, L10603 (2012).
7. Cheng, L. et al. Improved estimates of ocean heat content from 1960 to 2015. *Sci. Adv.* **3**, e1601545 (2017).
8. Johnson, G. et al. Ocean heat content [in State of the Climate 2012]. *Bull. Am. Meteorol. Soc.* **94**, S50–S53 (2013).
9. Meyssignac, B. et al. Measuring global ocean heat content to estimate the Earth energy imbalance. *Front. Mar. Sci.* https://doi.org/10.3389/fmars.2019.00432 (2019).
10. Balmaseda, M., Anderson, D. & Vidard, A. Impact of Argo on analyses of the global ocean. *Geophys. Res. Lett.* https://doi.org/10.1029/2007GL030452 (2007).
11. Abraham, J. P. A review of global ocean temperature observations: Implications for ocean heat content estimates and climate change. *Rev. Geophys.* **51**, 450–483 (2013).
12. Roemmich, D. et al. Unabated planetary warming and its ocean structure since 2006. *Nat. Clim. Chang.* **5**, 240–245 (2015).
13. Purkey, S. G. & Johnson, G. C. Warming of global abyssal and deep Southern Ocean waters between the 1990s and 2000s: contributions to global heat and sea level rise budgets. *J. Clim.* **23**, 6336–6351 (2010).
14. Kouketsu, S. et al. Deep ocean heat content changes estimated from observation and reanalysis product and their influence on sea level change. *J. Geophys. Res. Oceans* https://doi.org/10.1029/2010JC006464 (2011).
15. Gebbie, G. Atlantic warming since the Little Ice Age. *Oceanography* **32**, 220–230 (2019).
16. Zanna, L., Khatiwala, S., Gregory, J. M., Ison, J. & Heimbach, P. Global reconstruction of historical ocean heat storage and transport. *Proc. Natl Acad. Sci. USA* **116**, 1126–1131 (2019).
17. Bagnell, A. & DeVries, T. 20th century cooling of the deep ocean contributed to delayed acceleration of Earth's energy imbalance. *Nat. Commun.* **12**, 4604 (2021).
18. Johnson, G. C. & Lyman, J. M. Warming trends increasingly dominate global ocean. *Nat. Clim. Chang.* **10**, 757 (2020).
19. Hurrell, J. W. & Loon, Van H. Decadal variations in climate associated with the North Atlantic Oscillation. *Clim. Change* **36**, 301–326 (1997).
20. Knight, J. R. A signature of persistent natural thermohaline circulation cycles in observed climate. *Geophys. Res. Lett.* **32**, L20708 (2005).
21. IPPC. *Climate Change 2013: The Physical Science Basis* (Cambridge Univ. Press, 2013). (2013).
22. Irving, D. B., Wijffels, S. & Church, J. A. Anthropogenic aerosols, greenhouse gases, and the uptake, transport, and storage of excess heat in the climate system. *Geophys. Res. Lett.* **46**, 4894–4903 (2019).

23. Wijffels, S., Roemmich, D., Monselesan, D., Church, J. & Gilson, J. Ocean temperatures chronicle the ongoing warming of Earth. *Nat. Clim. Chang.* **6**, 116–118 (2016).
24. Rathore, S., Bindoff, N. L., Phillips, H. E. & Feng, M. Recent hemispheric asymmetry in global ocean warming induced by climate change and internal variability. *Nat. Commun.* **11**, 2008 (2020).
25. Tsubouchi, T. et al. Increased ocean heat transport into the Nordic Seas and Arctic Ocean over the period 1993–2016. *Nat. Clim. Chang.* **11**, 21–26 (2021).
26. Cheng, L. et al. Upper ocean temperatures hit record high in 2020. *Adv. Atmos. Sci.* **38**, 523–530 (2021).
27. Bryden, H. L. & Hall, M. M. Heat transport by currents across 25°N latitude in the Atlantic Ocean. *Science* **207**, 884–886 (1980).
28. Bryden, H. L., Longworth, H. R. & Cunningham, S. A. Slowing of the Atlantic meridional overturning circulation at 25° N. *Nature* **438**, 655–657 (2005).
29. Roemmich, D. & Wunsch, C. Two transatlantic sections: meridional circulation and heat flux in the subtropical North Atlantic Ocean. *Deep Sea Res. Part A. Oceanogr. Res. Pap.* **32**, 619–664 (1985).
30. Atkinson, C. P., Bryden, H. L., Cunningham, S. A. & King, B. A. Atlantic transport variability at 25° N in six hydrographic sections. *Ocean Sci.* **8**, 497–523 (2012).
31. Smeed, D. et al. Atlantic meridional overturning circulation observed by the RAPID-MOCHA-WBTS (RAPID-Meridional Overturning Circulation and Heatflux Array-Western Boundary Time Series) array at 26N from 2004 to 2018. https://doi.org/10.5285/8cd7e7bb-9a20-05d8-e053-6c86abc012c2 (2019).
32. Waugh, D. W. Relationships among tracer ages. *J. Geophys. Res.* **108**, 3138 (2003).
33. Holzer, M., Primeau, F. W., Smethie Jr., W. M. & Khatiwala, S. Where and how long ago was water in the western North Atlantic ventilated? Maximum entropy inversions of bottle data from WOCE line A20. *J. Geophys. Res. Ocean.* https://doi.org/10.1029/2009JC005750 (2010).
34. Levitus, S., Antonov, J. I., Boyer, T. P. & Stephens, C. Warming of the World Ocean. *Science* **287**, 2225 LP–2229 (2000).
35. Häkkinen, S., Rhines, P. B. & Worthen, D. L. Heat content variability in the North Atlantic Ocean in ocean reanalyses. *Geophys. Res. Lett.* **42**, 2901–2909 (2015).
36. Durack, P. et al. Ocean warming: from the surface to the deep in observations and models. *Oceanography* **31**, 41–51 (2018).
37. Tung, K.-K. & Zhou, J. Using data to attribute episodes of warming and cooling in instrumental records. *Proc. Natl Acad. Sci. USA* **110**, 2058 LP–2052063 (2013).
38. Folland, C. K., Boucher, O., Colman, A. & Parker, D. E. Causes of irregularities in trends of global mean surface temperature since the late 19th century. *Sci. Adv.* **4**, eaao5297 (2018).
39. Trenberth, K. E. & Shea, D. J. Atlantic hurricanes and natural variability in 2005. *Geophys. Res. Lett.* https://doi.org/10.1029/2006GL026894 (2006).
40. Roemmich, D. & Wunsch, C. Apparent changes in the climatic state of the deep North Atlantic Ocean. *Nature* **307**, 447–450 (1984).
41. Levitus, S. Interpentadal variability of temperature and salinity in the deep North Atlantic, 1970–1974 versus 1955–1959. *J. Geophys. Res. Oceans* **94**, 16125–16131 (1989).
42. Bryden, H. L. et al. Decadal changes in water mass characteristics at 24°N in the subtropical North Atlantic Ocean. *J. Clim.* **9**, 3162–3186 (1996).
43. Desbruyères, D. G., Purkey, S. G., McDonagh, E. L., Johnson, G. C. & King, B. A. Deep and abyssal ocean warming from 35 years of repeat hydrography. *Geophys. Res. Lett.* **43**, 10.356–10.365 (2016).
44. Allison, L. C. et al. Towards quantifying uncertainty in ocean heat content changes using synthetic profiles. *Environ. Res. Lett.* **14**, 84037 (2019).
45. Hurrell, J. W., Kushnir, Y., Ottersen, G. & Visbeck, M. in *The North Atlantic Oscillation* 1–36 (Wiley, 2003).
46. Visbeck, M. et al. *The North Atlantic Oscillation: Climatic Significance and Environmental Impact* (Wiley, 2003).
47. Dickson, R., Lazier, J., Meincke, J., Rhines, P. & Swift, J. Long-term coordinated changes in the convective activity of the North Atlantic. *Prog. Oceanogr.* **38**, 241–295 (1996).
48. Deser, C., Alexander, M. A., Xie, S.-P. & Phillips, A. S. Sea surface temperature variability: patterns and mechanisms. *Ann. Rev. Mar. Sci* **2**, 115–143 (2010).
49. Alekseev, G. V., Johannessen, O. M., Korablev, A. A., Ivanov, V. V. & Kovalevsky, D. V. Interannual variability in water masses in the Greenland Sea and adjacent areas. *Polar Res.* **20**, 201–208 (2001).
50. Hall, T. & Haine, T. On ocean transport diagnostics: the idealized age tracer and the age spectrum. *J. Phys. Oceanogr.* **32**, 1987–1991 (2002).
51. van Sebille, E. et al. Propagation pathways of classical Labrador Sea water from its source region to 26°N. *J. Geophys. Res. Oceans* **116**, C12027 (2011).
52. Yashayaev, I. & Loder, J. W. Recurrent replenishment of Labrador Sea Water and associated decadal-scale variability. *J. Geophys. Res. Oceans* **121**, 8095–8114 (2016).
53. Kim, W. M., Yeager, S. & Danabasoglu, G. Revisiting the causal connection between the great salinity anomaly of the 1970s and the shutdown of Labrador Sea deep convection. *J. Clim.* **34**, 675–696 (2021).
54. Zunino, P., Mercier, H. & Thierry, V. Why did deep convection persist over four consecutive winters (2015–2018) southeast of Cape Farewell? *Ocean Sci.* **16**, 99–113 (2020).
55. Cook, E. R., D'Arrigo, R. D. & Mann, M. E. A well-verified, multiproxy reconstruction of the winter North Atlantic Oscillation Index since a.d. 1400. *J. Clim.* **15**, 1754–1764 (2002).
56. Mellado-Cano, J., Barriopedro, D., García-Herrera, R., Trigo, R. M. & Hernández, A. Examining the North Atlantic Oscillation, East Atlantic Pattern, and Jet Variability since 1685. *J. Clim.* **32**, 6285–6298 (2019).
57. Dickson, R. R. et al. The Arctic Ocean response to the North Atlantic oscillation. *J. Clim.* **13**, 2671–2696 (2000).
58. Robson, J. I., Sutton, R. T. & Smith, D. M. Initialized decadal predictions of the rapid warming of the North Atlantic Ocean in the mid 1990s. *Geophys. Res. Lett.* https://doi.org/10.1029/2012GL053370 (2012).
59. Caesar, L., Rahmstorf, S. & Feulner, G. On the relationship between Atlantic meridional overturning circulation slowdown and global surface warming. *Environ. Res. Lett.* **15**, 24003 (2020).
60. Smeed, D. A. et al. The North Atlantic Ocean is in a state of reduced overturning. *Geophys. Res. Lett.* **45**, 1527–1533 (2018).
61. Johnson, G. C. et al. Ocean heat content [in "State of the Climate in 2019," Chapter 3]. *Bull. Am. Meteorol. Soc.* **101**, s140–s144 (2020).
62. Key, R. M. et al. A global ocean carbon climatology: results from Global Data Analysis Project (GLODAP). *Glob. Biogeochem. Cycles* https://doi.org/10.1029/2004GB002247 (2004).
63. Mishonov, A. & National Center for Atmospheric Research Staff. (eds) The Climate Data Guide: World Ocean Atlas 2013 (WOA13). https://climatedataguide.ucar.edu/climate-data/world-ocean-atlas-2013-woa13 (2016).
64. Lauvset, S. K. et al. A new global interior ocean mapped climatology: the 1° × 1° GLODAP version 2. *Earth Syst. Sci. Data* **8**, 325–340 (2016).
65. Rubin, S. I. & Key, R. M. Separating natural and bomb-produced radiocarbon in the ocean: the potential alkalinity method. *Glob. Biogeochem. Cycles* **16**, 19–52 (2002).
66. Shao, A. E., Mecking, S., Thompson, L. & Sonnerup, R. E. Mixed layer saturations of CFC-11, CFC-12, and SF6 in a global isopycnal model. *J. Geophys. Res. Oceans* **118**, 4978–4988 (2013).
67. Good, S. A., Martin, M. J. & Rayner, N. A. EN4: Quality controlled ocean temperature and salinity profiles and monthly objective analyses with uncertainty estimates. *J. Geophys. Res. Oceans* **118**, 6704–6716 (2013).
68. Huang, B. et al. Extended reconstructed sea surface temperature, version 5 (ERSSTv5): upgrades, validations, and intercomparisons. *J. Clim.* **30**, 8179–8205 (2017).
69. Gebbie, G. & Huybers, P. The Little Ice Age and 20th-century deep Pacific cooling. *Science* **363**, 70–74 (2019).
70. Ishii, M. et al. Accuracy of global upper ocean heat content estimation expected from present observational data sets. *SOLA* **13**, 163–167 (2017).
71. Haine, T. W. N. & Hall, T. M. A generalized transport theory: water-mass composition and age. *J. Phys. Oceanogr.* **32**, 1932–1946 (2002).
72. Jaynes, E. T. Information theory and statistical mechanics. *Phys. Rev.* **106**, 620–630 (1957).
73. Khatiwala, S., Primeau, F. & Hall, T. Reconstruction of the history of anthropogenic CO2 concentrations in the ocean. *Nature* **462**, 346–349 (2009).
74. Stuiver, M., Quay, P. D. & Ostlund, H. G. Abyssal water carbon-14 distribution and the age of the world oceans. *Science* **219**, 849–851 (1983).
75. Matsumoto, K. Radiocarbon-based circulation age of the world oceans. *J. Geophys. Res. Oceans* https://doi.org/10.1029/2007JC004095 (2007).
76. Fine, R. A. Observations of CFCs and SF6 as ocean tracers. *Ann. Rev. Mar. Sci.* **3**, 173–195 (2011).
77. Wunsch, C. Oceanic age and transient tracers: analytical and numerical solutions. *J. Geophys. Res. Ocean.* **107**, 1–18 (2002).
78. Holzer, M. & Hall, T. M. Transit-time and tracer-age distributions in geophysical flows. *J. Atmos. Sci.* **57**, 3539–3558 (2000).
79. Haine, T. On tracer boundary conditions for geophysical reservoirs: How to find the boundary concentration from a mixed condition. *J. Geophys. Res.* https://doi.org/10.1029/2005JC003215 (2006).
80. Tomczak, M. A multi-parameter extension of temperature/salinity diagram techniques for the analysis of non-isopycnal mixing. *Prog. Oceanogr.* **10**, 147–171 (1981).
81. Darryn, W., Francois, P., Tim, D. & Mark, H. Recent changes in the ventilation of the Southern Oceans. *Science* **339**, 568–570 (2013).
82. Jackson, L. C. et al. The evolution of the North Atlantic Meridional Overturning Circulation since 1980. *Nat. Rev. Earth Environ.* https://doi.org/10.1038/s43017-022-00263-2 (2022).
83. Lund, D. C., Lynch-Stieglitz, J. & Curry, W. B. Gulf Stream density structure and transport during the past millennium. *Nature* **444**, 601–604 (2006).
84. Caesar, L., McCarthy, G. D., Thornalley, D. J. R., Cahill, N. & Rahmstorf, S. Current Atlantic Meridional Overturning Circulation weakest in last millennium. *Nat. Geosci.* **14**, 118–120 (2021).

85. Morarji, N. *Variability and Transport Methodology of the Atlantic Meridional Overturning Circulation at 26°N*. Doctoral thesis, Univ. of Southampton (2019).
86. Hurrell, J. & National Center for Atmospheric Research Staff. (eds) The Climate Data Guide: Hurrell North Atlantic Oscillation (NAO) Index (station-based). https://climatedataguide.ucar.edu/climate-data/hurrell-north-atlantic-oscillation-nao-index-station-based (2020).
87. Cheng, L. & Zhu, J. Benefits of CMIP5 multimodel ensemble in reconstructing historical ocean subsurface temperature variations. *J. Clim.* **29**, 5393–5416 (2016).
88. Rahmstorf, S. Ocean circulation and climate during the past 120,000 years. *Nature* **419**, 207–214 (2002).
89. Yao, S.-L., Luo, J.-J., Huang, G. & Wang, P. Distinct global warming rates tied to multiple ocean surface temperature changes. *Nat. Clim. Chang.* **7**, 486–491 (2017).
90. Caesar, L., Rahmstorf, S., Robinson, A., Feulner, G. & Saba, V. Observed fingerprint of a weakening Atlantic Ocean overturning circulation. *Nature* **556**, 191–196 (2018).
91. Bryden, H. L. et al. Reduction in ocean heat transport at 26°N since 2008 cools the eastern subpolar gyre of the North Atlantic Ocean. *J. Clim.* **33**, 1677–1689 (2020).

Acknowledgements

M.-J.M. was supported by the University of Exeter and by the UKRI grant No NE/P0190064/1 under the project TICTOC (Transient tracer-based Investigation of Circulation and Thermal Ocean Change). H.M. was supported by CNRS. Calculations were performed on Ifremer's DATARMOR supercomputer. M.-J.M. acknowledges conversations with T. Tudino and also thanks him for participating in the 2015 cruise.

Author contributions

M.-J.M. performed the transient tracer measurements for the 2010 and 2015 cruises and wrote the initial manuscript draft. H.M. conducted the calculations. Both authors designed the study and contributed to the analysis, interpretation of the results and to improvement of the manuscript.

Competing interests

The authors declare no competing interests.

Additional information

Supplementary information The online version contains supplementary material available at https://doi.org/10.1038/s43247-022-00443-4.

Correspondence and requests for materials should be addressed to Marie-José. Messias.

Peer review information *Communications Earth & Environment* thanks the anonymous reviewers for their contribution to the peer review of this work. Primary handling editors: Regina Rodrigues and Clare Davis.